Size-Dependent Electrostatic Adsorption of Polymer-Grafted Gold Nanoparticles on Polyelectrolyte Brushes

Ye Chan Kim[1], Son Hoang[1], Karen I. Winey[1,2], and Russell J. Composto[1*]*

[1]Department of Materials Science and Engineering, University of Pennsylvania, Philadelphia, Pennsylvania 19104, United States

[2]Department of Chemical and Biomolecular Engineering, University of Pennsylvania, Philadelphia, Pennsylvania 19104, United States

KEYWORDS polyelectrolyte brushes, gold nanoparticles, electrostatic interaction, adsorption, size separation

ABSTRACT

Designing a functional surface that selectively adsorbs nanoparticles based on their size and shape is essential for developing an advanced adsorption-based, post-synthesis nanoparticle separation device. We demonstrate selective adsorption of larger nanoparticles from solution onto a polyelectrolyte brush by tuning the salt concentration. Specifically, a positively-charged polyelectrolyte brush is created by converting pyridine groups of poly(2-vinylpyridine) to *n*-methyl pyridinium groups using methyl iodide. The adsorption kinetics and thermodynamics of polyethylene glycol-grafted, negatively charged gold nanoparticles (diameters of 12 and 20 nm) were monitored as a function of salt concentration. In a salt-free solution, the polyelectrolyte brush adsorbs gold nanoparticles of both sizes. As the salinity increases, the areal number density of adsorbed nanoparticles monotonically decreases and becomes negligible at high salinity. Interestingly, there is an intermediate range of salt concentrations (*i.e.*, 15 − 20 mM of NaCl) where the decrease in nanoparticle adsorption is more pronounced for smaller particles, leading to size-selective adsorption of the larger nanoparticles. As a further demonstration of selectivity, the polyelectrolyte brush is immersed in a binary mixture of 12-nm and 20-nm nanoparticles and found to selectively capture larger particles with ~ 90 % selectivity. In addition, the size distribution of as-synthesized gold nanoparticles, with an average diameter of 12 nm, was reduced by selectively removing larger particles by exposing the solution to polyelectrolyte brush surfaces. This study demonstrates the potential of a polyelectrolyte brush separation device to remove larger nanoparticles by controlling electrostatic interactions between polymer brushes and particles.

INTRODUCTION

Nanoparticles with uniform size and shape are crucial for advanced nanoparticle-based technologies such as biosensing,[1-3] photonics,[4, 5] photovoltaics,[6-8] and optoelectronics[9, 10] applications. These techniques exploit the unique optical properties (*e.g.*, plasmon resonances) of nanoparticles, whose properties are determined by size and shape at the nanometer scale,[11] and thus require very narrow distributions. However, typical synthesis routes often fail to produce monodisperse nanoparticles and yield a small number of nonspherical particles that deviate from the target size and shape. One approach to reduce this dispersity is post-synthesis separation. For instance, various nanoparticle separation methods have been studied, including dialysis,[12] electrophoresis,[13], and centrifugation.[14-17] Although these efforts have potential, the development of a scalable and continuous method to separate nanoparticles with high efficiency and resolution has not yet been realized.

To address these challenges, we can consider the design of a separation system that selectively adsorbs nanoparticles as they pass through a chromatography column.[18] In adsorption-based separation processes, nanoparticles with a specific size and shape are selectively adsorbed to the surface of the medium, so that only the desired nanoparticles ultimately pass through. A longer-term goal, beyond the scope of the present study, is to release the adsorbed particles to regenerate the surface. To realize this strategy, it is essential to tailor the nanoparticles-surface interactions which depend on the properties of nanoparticles and surface.

In general, nanoparticles dispersed in an aqueous solution exhibit a charged surface, and thus, exposure of these nanoparticles to an oppositely charged polyelectrolyte (PEL) brush coating a surface is a promising approach to control the adsorption thermodynamics of nanoparticles.[19, 20] PEL brushes are surface-tethered polymer chains consisting of charged monomers. Specifically,

the properties of PEL brushes can be tailored by varying charge fraction,[21, 22] molecular weight,[23, 24] grafting density,[25-28] chemical structure,[29] and counterion species.[30-34] Nanoparticle adsorption on a brush can be controlled by varying individual or combinations of these parameters. Experiments[35-37] and simulations[38-40] have been performed to understand how the insertion of nanoparticles into a polymer bush depends on these parameters. To briefly summarize these findings, a polymer brush with a moderate areal number density of chains that strongly interact with nanoparticles provides the optimum conditions for particles to penetrate and adsorb into the brush. However, a low areal number of chains presents too few interactions with attractive nanoparticles, whereas a high areal number of chains results in steric repulsion of nanoparticles.

Nanoparticle-PEL brush interactions can be further controlled by external stimuli such as pH, salt concentration, and temperature. For instance, our recent study demonstrated that a pH-responsive weak PEL brush can selectively adsorb citrate-coated gold nanoparticles (AuNPs) according to their size by adjusting the buffer pH.[41] At low pH, a highly swollen polymer brush strongly attracts AuNPs, irrespective of size, resulting in no size selectivity between smaller, 11-nm, and larger, 21-nm, nanoparticles. In contrast, at neutral pH, a slightly swollen polymer brush presenting weak interactions with the nanoparticles is unfavorable towards the penetration of larger nanoparticles, resulting in preferential adsorption of smaller nanoparticles.

Here, we investigate the potential of strong PEL brushes to separate nanoparticles by size. Specifically, we aim to selectively remove larger nanoparticles because most synthesis methods result in a log-normal distribution[42] with a tail of larger nanoparticles that deviate greatly from the average size. Based on our recent study,[41] we have designed a model PEL brush-nanoparticle system that preferentially removes larger nanoparticles from polydisperse samples. System characteristics and conditions are as follows. First, the PEL brush should be highly swollen in

water to maximize the insertion of large nanoparticles into the interior of the brush. Second, the size-dependent interaction between nanoparticles and PEL brushes should be controlled by external stimuli. Conditions must be chosen such that attractive interactions between the small nanoparticles and polymer brushes are negligible, whereas between larger nanoparticles and polymer brushes should be sufficient to adsorb nanoparticles. Note that the strength of this interaction will dictate whether the brush surface is reusable. Furthermore, the conformation of the polymer brush should remain constant in the presence of external stimuli; namely, only the size-dependent attractive force should be dependent on the external stimuli.

In this paper, we demonstrate that a positively charged strong PEL brush can selectively adsorb larger nanoparticles from a solution of negatively charged, polymer-grafted spherical AuNPs in solution. We compare the adsorption behavior of 12-nm and 20-nm polyethylene glycol grafted (PEGylated) AuNPs on a polystyrene-*b*-poly(2-vinylpyridine) (PS-*b*-P2VP) brush where the outer P2VP brush is ~ 50 % quaternized. Solution salinity provides the external stimuli for controlling the electrostatic interaction between the brush surface and AuNPs. At low salinity, the electrostatic adsorption of both the 12-nm and 20-nm AuNPs is strong, and size selectivity is not observed. However, as salinity increases from 0 to 20 mM, the salt screens the electrostatic interactions between the brush and nanoparticle resulting in a monotonic decrease in the areal number density of both the smaller and larger AuNPs. However, increasing the salt concentration doesn't affect the conformation of the PEL brushes. When compared at the same salt concentrations, larger nanoparticles exhibit a higher areal number density than smaller ones which exhibit negligible adsorption at 15 mM and above. To test selectivity, absorption of a bimodal distribution was shown to exhibit increasing selectivity as salt concentration increases reaching ~ 90 % at 20 mM. For a more stringent test, a PEL brush was inserted into a solution of as-

synthesized AuNPs (average diameter of 12 nm) resulting in a significant narrowing of the size distribution. This study provides proof of concept that a separation device based on the PEL brush can effectively remove larger nanoparticles by controlling electrostatic interactions between brush and particle.

RESULTS AND DISCUSSION

Preparation of PEL Brush. In our previous study,[41] we developed a simple method for fabricating P2VP brushes using a symmetric PS-*b*-P2VP block copolymer (BCP), Figure 1a. Building upon this platform, we synthesize PEL brushes that exhibit a positive charge and hydrophilicity by converting some of the pyridine groups of P2VP to *n*-methylpyridinium (NMP^+) groups through a quaternization reaction. The PEL brush synthesis involves (1) a quaternization reaction that converts the P2VP brush into a P2VP/NMP^+ random copolymer brush and (2) performing anion exchange to produce a hydrophilic, positively charged PEL brush.

First, the reaction condition was optimized to effectively induce the quaternization of pyridines while maintaining the morphology of the BCP film. Previous studies have shown that pyridine can be converted to quaternary pyridinium salts via reaction with alkyl halides (*i.e.*, Menshukin reaction).[43] In particular, quaternized P2VP microdomains in self-assembled BCP structures were prepared using alkyl halides introduced from the solution or a gas phase.[44-47] Here, partially converted P2VP/NMP^+I^- PEL brushes, as depicted in Figure 1b, were synthesized by immersing P2VP brushes in a 10 v/v% methyl iodide solution for 24 hours. Hexane prevents the dissolution of the BCP into solution, while methyl iodide penetrates the P2VP domains to initiate the reaction. The BCP monolayer remains intact throughout the reaction. Figure S1 demonstrates how the ratio of hexane and methyl iodide affects film stability. The 10 v/v% ratio represents an

optimized mixture, consistent with other studies using different alkyl halides (*e.g.*, ethyl bromide).[44]

In the second step, anion exchange was performed to generate highly hydrophilic PEL brushes. The hydrophilicity of these PEL brushes is known to depend on the type of counterions.[30] The as-synthesized PEL brushes contain iodide counter anions that interact with the quaternary pyridinium groups through strong ion pairing. Such ion-specific interactions make the PEL brushes more hydrophobic which limits the range of electrostatic forces for nanoparticle adsorption. To enhance hydrophilicity, anion exchange is performed by immersing PEL brushes in a 0.1 M NaCl solution for 30 minutes followed by rinsing with DI water for another 30 minutes. Figure 1c shows the P2VP/NMP^+Cl^- brush that provides a tunable surface for interacting with negatively charged nanoparticles.

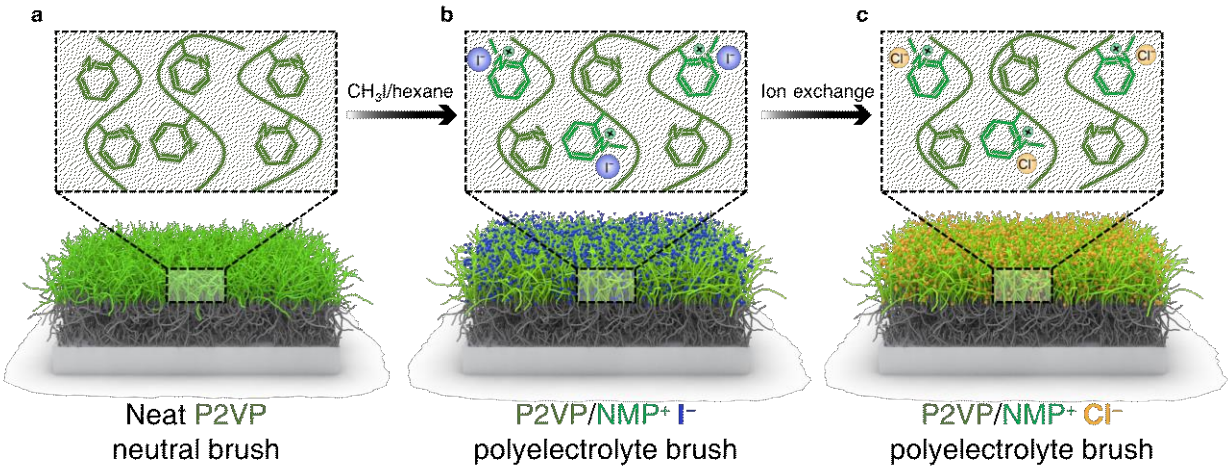

Figure 1. Schematics of the PEL brush preparation on a Si wafer. (a) Neat P2VP brush constructed from a PS-*b*-P2VP (PS layer, gray, P2VP layer, green). **(b)** PEL brush after converting pyridine groups into NMP^+ groups (iodide anions, blue). **(c)** PEL brush after counterion exchange with chloride anions (yellow).

Characterization of PEL Brush. The charge fraction, counter anion species, and brush structure at each step of PEL brush synthesis were determined. First, we investigated whether the methyl iodide could sufficiently penetrate the P2VP domains and react with pyridine groups, given that the BCP chain does not dissolve in the hexane mixture. To do this, the BCP was drop-cast onto a Si wafer, resulting in a coating of several micrometers in thickness. Subsequently, thermal annealing was performed, followed by the quaternization reaction and ion exchange process. Figure 2a shows FT-IR spectra from the neat PS-*b*-P2VP bulk film with two adsorption peaks at 1590 cm^{-1} and 1570 cm^{-1}, corresponding to the two distinct modes of ring-breathing vibrations of pyridine groups. These vibration modes shift to a higher frequency when the lone pair of nitrogen coordinates or binds to any electron-accepting groups.[48] We can observe this shift after quaternizing pyridine groups with methyl iodides (blue, Figure 2a) as noted by the appearance of adsorption peaks at 1628 cm^{-1} and 1580 cm^{-1} which correspond to the two ring-breathing vibration modes of pyridinium groups. Notably, the vibration modes of pyridine groups remain after the reaction, suggesting an incomplete conversion of pyridine groups to NMP^+ groups. It can be understood that the nitrogen atoms at the *ortho* position are sterically hindered, which limits the access of methyl iodide molecules. The quaternized pyridinium groups remained after performing anion exchange (yellow, Figure 2a). FT-IR spectra also support the formation of charged groups in the P2VP domain in the frequency range from 3000 cm^{-1} to 4000 cm^{-1}. As shown in Figure S2, a broad O-H stretch peak is observed at 3446 cm^{-1} after quaternization, implying the formation of hydrated charged groups. Interestingly, the O-H stretch peak becomes stronger and shifts to a shorter frequency at 3370 cm^{-1} after anion exchange with chloride, implying stronger hydration of the charged groups. The successful quaternization of pyridine groups is consistent with the effective penetration of methyl iodide within BCP bulk samples.

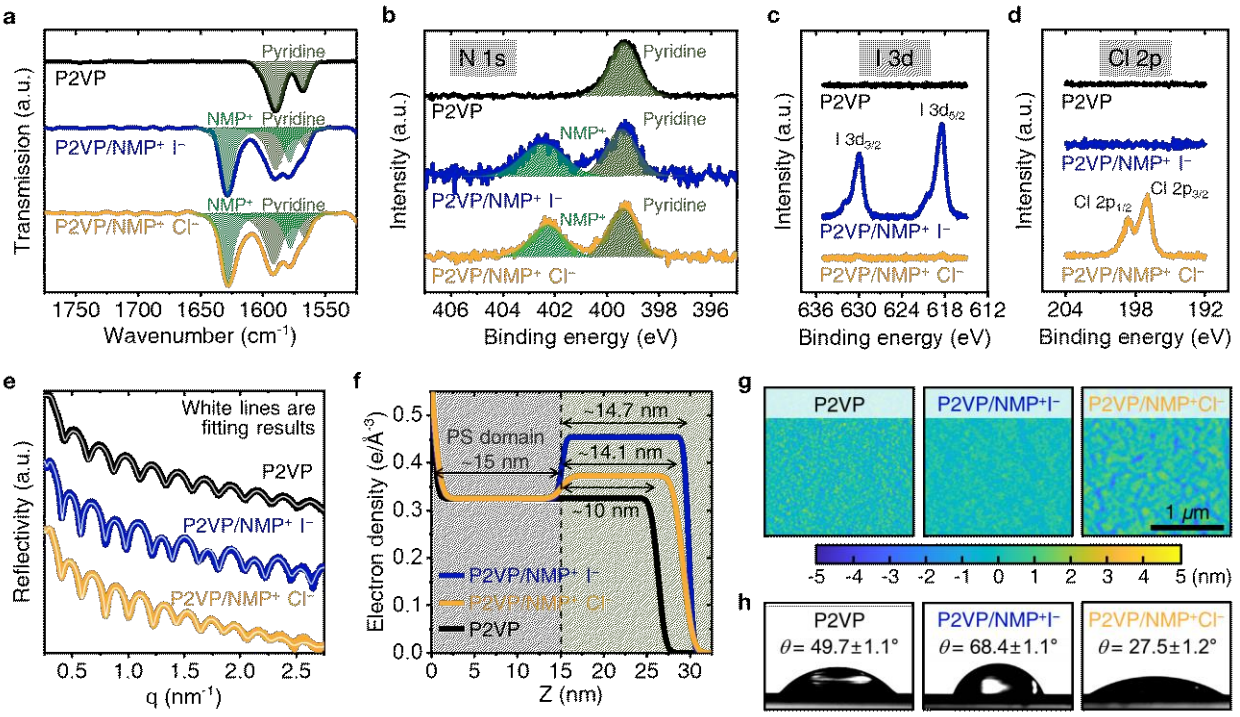

Figure 2. Characterization of dry PEL brushes constructed from a PS-*b*-P2VP. (a) FT-IR spectra, **(b)** N 1s, **(c)** I 3d, and **(d)** Cl 2p XPS spectra, **(e)** XRR profiles, **(f)** electron density profiles along the out-of-plane direction (Z), **(g)** AFM height images, and **(h)** photos of water droplets on the P2VP, P2VP/NMP$^+$I$^-$, and P2VP/NMP$^+$Cl$^-$ brushes. Fitting results for pyridine and NMP$^+$ are shown in dark green and green in (a) and (b), respectively. The numbers in (h) are the polymer brush surfaces' water contact angles, θ.

To further demonstrate the successful formation of the PEL brushes, X-ray photoelectron spectroscopy (XPS) was performed. As shown in Figure 2b, the neat P2VP brush shows a nitrogen signal corresponding to the pyridine group's nitrogen at the binding energy of 399.3 eV. The quaternization of the pyridine groups leads to a change in the oxidation state of nitrogen atoms, resulting in a peak shift. As expected, after the quaternization, the nitrogen XPS peak shifts to a higher binding energy at 402.5 eV, corresponding to the pyridinium groups' positively charged nitrogen atoms. The residual N 1s XPS peak for pyridine indicates incomplete conversion of pyridine to pyridinium, which is consistent with FT-IR spectra of bulk BCP films. Based on the XPS peak area ratio of pyridine and pyridinium, the charge fraction of the PEL brush was ~ 50 %.

The anion exchange process does not affect the charge fraction (yellow, Figure 2b). The successful quaternization reaction is also confirmed by the I 3d XPS spectra, Figure 2c. The two distinct XPS peaks correspond to the two different spin states (*i.e.*, $3d_{3/2}$ and $3d_{5/2}$) of iodide anions observed after the reaction, which indicates the successful reaction between pyridine groups and methyl iodide. In addition, the iodide XPS peaks disappear, and chloride XPS peaks (*i.e.*, Cl $2p_{1/2}$ and Cl $2p_{3/2}$) appear after the anion exchange, indicating complete ion exchange from iodide to chloride (Figures 2c and 2d). To sum up, the XPS analysis demonstrates the successful formation of the P2VP/NMP^+Cl^- brush by the quaternization of the neat P2VP brush followed by anion exchange.

Although the XPS analysis provides important information about the PEL brushes, more is needed to characterize the entire PEL brush because the XPS spectra represents only the outermost layer (~ 5 nm) of the PEL brush. To characterize the entire PEL brush along the out-of-plane direction, X-ray reflectivity (XRR) was performed, Figure 2e. The XRR profiles for P2VP, P2VP/NMP^+I^-, and P2VP/NMP^+Cl^- brushes were fit using a two-layer model consisting of a PS underlayer and a PEL brush layer. From these fits, the electron density profiles of each polymer brush were obtained in the out-of-plane direction of the film (Figure 2f). Consistent with our previous results,[41] XRR cannot distinguish the electron density difference between the P2VP and the PS layers; for this unlabeled case, XPS can only confirm that the total film thickness is 25 nm. (black, Figure 2f). However, the quaternization reaction significantly enhances electron density contrast between the PS layer and the P2VP/NMP^+I^- brush layer due to heavy atoms (*i.e.*, iodide anions) in the brush. Based on this, the height of the PS layer was found to be 15 nm, and the height of the P2VP/NMP^+I^- brush was found to increase to 14.7 nm due to the increase in molecular weight relative to the 10-nm thick P2VP brush. Here, we note two important observations. First, the constant electron density with brush height indicates a uniform

quaternization reaction throughout the brush. Second, as confirmed by the AFM images in Figure 2g, the selective increase in molecular weight of one block of the BCP does not disrupt the lateral uniformity of the brush. This suggests that the BCP layer remained intact during the quaternization reaction.

The hydrophilicity of the brush surface decreases from the neutral P2VP brush (contact angle, $\theta = 49.7°$) to the P2VP/NMP$^+$I$^-$ brush ($\theta = 68.4°$), as expected, Figure 2h. The ion exchange process from iodide to chloride successfully reduces the contact angle to 27.5°. Consistent with these results, ion exchange from iodide to chloride (a relatively lighter element compared to iodine), XRR finds a decrease in electron density and a slightly smaller brush thickness of 14.1 nm, Figure 2f. While the surface roughness of dried films does not reflect the brush height uniformity when swollen, we note that the root-mean-square roughness is < 1 nm, indicating smooth surfaces throughout the chemical transformations.

Effect of Salt Concentration on the PEL brush and PEGylated AuNPs. Next, we investigate the characteristics (*i.e.*, charge state, hydration state, and structure) of positively charged PEL brushes and negatively charged PEGylated AuNPs in aqueous solutions as a function of salt concentrations to gain insight into brush-nanoparticle interactions. According to Debye-Hückel theory[49] and experiments,[50, 51] the electrostatic interaction between charged species can be modulated by the addition of salt. In general, an increase in salt concentration alters the ion distribution and electric double-layer structure on charged surfaces. As a result, electrostatic attraction is reduced by a screening effect that prevents the electric potential from persisting over long distances. In addition to electrostatic forces, the presence of salts in the solution may also influence the structure of polymer brushes, potentially affecting the adsorption of nanoparticles. Thus, in this study, we use salt concentration as the independent variable to investigate how the

characteristics of PEL brushes and nanoparticles change. Consequently, based on these changes, we aim to determine whether we can control the adsorption of nanoparticles onto (into) the PEL brush.

First, we determine the characteristic sizes of PEL brushes and PEGylated AuNPs. As shown in Figure 3a, the PEL brush height is monitored as a function of immersion time by *in situ* ellipsometry. The brush thickness in the dry state is measured to be 15 nm, which agrees with the XRR result. When the PEL brush is immersed in water, the PEL brush height rapidly increases and equilibrates at ~ 46 nm. The height of the swollen polymer brush was further monitored as salt concentration was increased in intervals of 5 mM up to 20 mM. Within this range of salt concentrations, Figure 3a shows that the brush height decreases very slightly while remaining swollen. The observation suggests that these PEL brushes exist within the osmotic brush region described by polymer brush theory[52] and, thus, remain in a swollen state due to the osmotic pressure resulting from counterions and polymer-solvent interactions.

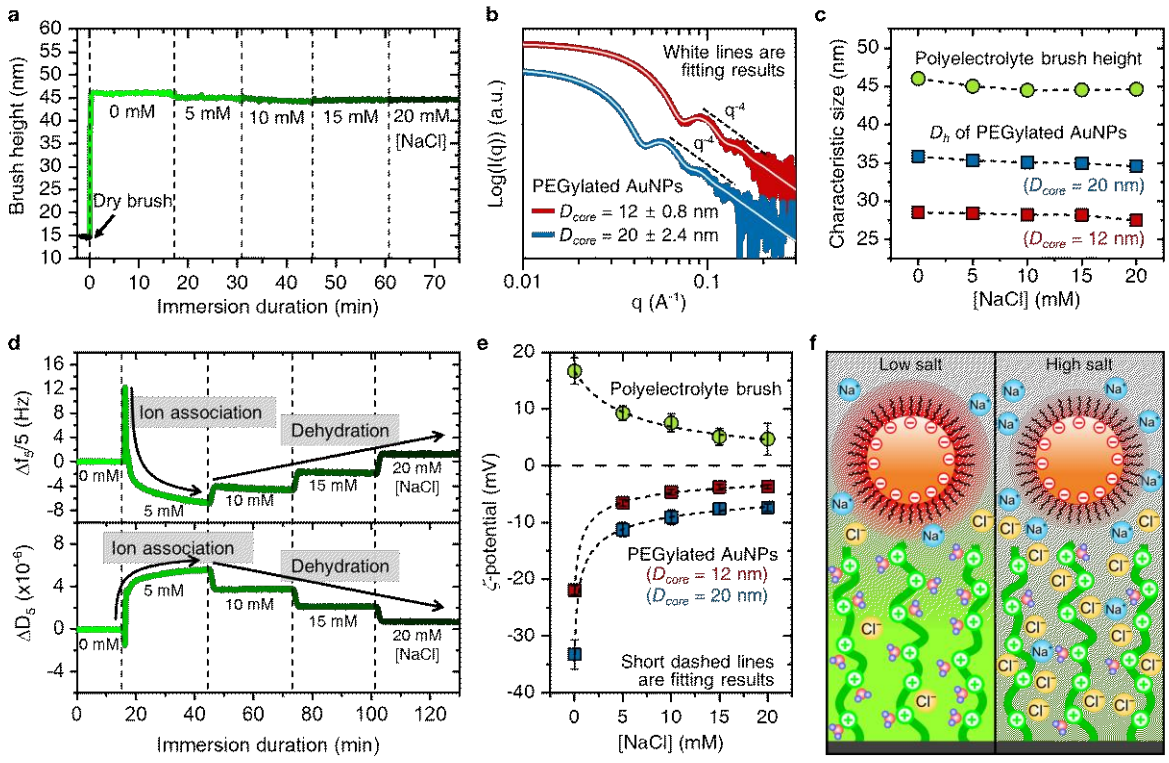

Figure 3. Effect of salt on the wet PEL brush and PEGylated AuNPs. **(a)** In situ brush thickness as a function of immersion time. **(b)** SAXS 1D profiles of PEGylated AuNPs. **(c)** The characteristic size of PEL brushes (circles) and PEGylated AuNPs (squares) as a function of salt concentration. **(d)** In situ change in resonant frequency and dissipation factor of the 5th overtone as a function of immersion time. **(e)** ζ-potential of PEL brush (circles) and PEGylated AuNPs (squares) as a function of salt concentration. **(f)** Schematics of PEL brushes and PEGylated AuNPs at low salt (left) and high salt (right) concentrations.

Next, we characterize the size of PEGylated AuNPs at salt concentrations from 5mM to 20mM. The PEGylated 12-nm and 20-nm AuNPs were synthesized using the modified Frens[53, 54] and seeded growth methods.[55] The core size of AuNPs is characterized by small-angle X-ray scattering (SAXS), Figure 3b. The decay of scattering intensity proportional to q^{-4} at the high q range and the plateau observed at the low q range indicate successful synthesis of spherical nanoparticles stably dispersed in the aqueous solution. Using the Schultz polydisperse model[56, 57], fits to the scattering intensities determine mean diameters of 12 ± 0.8 nm and 20 ± 2.4 nm. The

AuNPs grafted with PEG brushes used in this study are stably dispersed at NaCl concentrations up to 20 mM, Figure S3. This stability is necessary for investigating PEGylated AuNP adsorption on (in) PEL brushes without nanoparticle aggregation. In addition to the core size and stability in solution, the hydrodynamic diameter, D_h, of PEGylated AuNPs was measured as a function of salt concentration using dynamic light scattering. Figure 3c shows the size of the nanoparticles and the height of the PEL brush as a function of salt concentration. The D_h of the 20-nm AuNPs is ~ 35 nm whereas the AuNPs with the smaller core is ~ 28 nm. Relative to the core, the hydrated PEG brush adds a similar thickness, namely ~ 7.5 nm, and ~ 8.0 nm, respectively to both nanoparticles. Additionally, due to the relatively high grafting density, the PEG brush thickness is invariant to changes in salt concentration, accounting for the nearly constant values of D_h shown in Figure 3c. Here, we note that 12-nm and 20-nm AuNPs have smaller D_h values than the height of swollen PEL brushes, ~ 45 nm. Thus, AuNPs of both sizes can sufficiently penetrate the brush. In summary, the thickness of the PEL brushes and the diameter of AuNPs are independent of salt concentration. Therefore, by varying the salt concentration, we can control particle adsorption solely by screening the electrostatic attraction between AuNPs and the PEL brush surface without perturbing the particle or brush size.

In contrast to their dimensions, the charge and hydration state of the PEL brush and PEGylated AuNPs depend on salt concentration. Using quartz crystal microbalance with dissipation (QCM-D), the normalized resonance frequency ($\Delta f_5/5$) and dissipation factor (ΔD_5) are used to investigate the effect of salt concentration on the hydration of PEL brushes as shown in Figure 3d. The change in resonant frequency indicates a mass change of the PEL brushes induced by the adsorption/desorption of species coupled to the PEL brushes. Thus, by observing the change in resonant frequency, hydration/dehydration and ionic association/dissociation of the PEL brush

can be monitored. When the solution surrounding the PEL brush is changed from a salt-free solution (lightest green) to NaCl 5 mM (darker green), a sharp increase is observed followed by a gradual decrease in $\Delta f_5/5$. This rapid increase suggests that a sudden increase in salinity leads to a rise in osmotic pressure and consequent dehydration of the PEL brush. The gradual decrease indicates a redistribution of ions into the PEL brush followed by their association with the charged groups in the brush. Upon incrementally increasing the salt concentration from 5 to 20 mM (light to dark green) the normalized resonance frequency monotonically increases indicating dehydration of the PEL brush and negligible change in ion association. The dehydration of the PEL brush as salt concentration increases is also reflected in the change in dissipation factor shown in Figure 3d, bottom. The dissipation factor is mainly affected by (1) the conformation of the PEL brush and (2) the friction between the PEL brush and the surrounding medium interacting with the PEL brush.[32, 58, 59] Because we already showed that PEL brush conformation does not depend on salt concentration up to 20 mM, we attribute the change in dissipation factor to the friction between PEL brush segments and the interacting molecules. As the PEL brush dehydrates upon increasing salt concentration, the friction at the PEL brush/water interface decreases. As a result, the energy loss of the oscillating QCM sensor decreases and, correspondingly, so does the dissipation factor. On the other hand, ion association increases the interfacial friction, producing an increase in energy loss and dissipation factor. To sum up, the change in resonant frequency and dissipation factor shows that increasing salt concentration leads to monotonic dehydration of the PEL brush. In terms of nanoparticle adsorption, the decrease in the number of water molecules participating in hydration reduces the number of molecules released by nanoparticle adsorption, which in turn, can inhibit nanoparticle adsorption.

In addition to the hydration state of the PEL brush, we further investigated the charge state of the PEL brush and PEGylated AuNPs using ζ-potential as a function of salt concentration (Figure 3e). The PEL brush exhibits a positive charge at all salt concentrations, and the ζ-potential exponentially decreases from 17.5 mV to 5 mV as salt concentration increases (green, Figure 3e). For the PEGylated AuNPs, the 12-nm and 20-nm AuNPs retain their negative charge even after PEGylation, consistent with the literature.[60-62] This negative charge can be attributed to residual citrate molecules on the surface of AuNPs and the inability of the relatively short PEG brush to screen this charge. Similar to the PEL brush, the absolute ζ-potential of PEGylated AuNPs exponentially decreases as salt concentration increases, with the most significant decrease between 0 and 5 mM (red and blue, Figure 3e). In sum, the PEL brush and PEGylated AuNPs exhibit positive and negative charges, respectively, and the charge screening increases as salt concentration increases.

Based on the characteristic size, hydration, and charge state of the PEL brush and PEGylated AuNPs, we can predict the PEL brush/AuNP interactions at low and high salt concentrations. At low salt concentrations (left, Figure 3f), the number of water molecules participating in the hydration of the PEL brush is large, and both the PEL brush and nanoparticles have a high charge. In this case, water molecules are released when AuNP adsorbs, resulting in a favorable increase in the translational entropy of the system. Moreover, due to strong electrostatic attraction, spontaneous adsorption of the AuNPs is expected. At high salt concentrations (right, Figure 3f), the adsorption of nanoparticles is expected to become thermodynamically less favorable due to the reduction in the number of water molecules that can be released and a weaker electrostatic attraction between the PEL brush and AuNPs due to the reduction their charge states.

These predictions will be tested in the next section by comparing the adsorption of 12-nm and 20-nm PEGylated AuNPs on the PEL brush surface.

Salt-Mediated Size-Dependent AuNP Adsorption. To investigate nanoparticle adsorption as a function of salt concentration, the adsorption of PEGylated AuNPs on the PEL brush was monitored in real time using QCM-D. Figures 4a and 4b show the changes in normalized resonant frequency during the adsorption of 12-nm and 20-nm PEGylated AuNPs. AuNP concentrations of 2000 pM and 500 pM for the 12-nm and 20-nm nanoparticles have similar particle mass fractions in solution. The decrease in the resonant frequency was greatest for both AuNPs in salt-free solutions, consistent with the strong electrostatic attraction between AuNPs and PEL brushes, and the favorable release of a large number of water molecules from the PEL brush. In addition, for both nanoparticle sizes, a monotonic decrease in the absolute value of the resonant frequency is observed as salt concentration increases. This is attributed to the decrease in the electrostatic attraction between the nanoparticles and the PEL brushes due to charge screening. The adsorption of nanoparticles, regulated by salt concentration, was observed regardless of nanoparticle size. This aligns with our expectations, demonstrating that the adsorption behavior of nanoparticles is governed by electrostatic interactions. Interestingly, at all salt concentrations, the 20-nm AuNPs exhibited a greater decrease in resonance frequency, indicating that the adsorption of larger nanoparticles is more favorable than the smaller ones. Using the 20 hrs values for both nanoparticles, Figure 4c shows the absolute values of the reduced resonance frequency decreasing with salt concentration. Because the decrease in resonance frequency is proportional to the mass of adsorbed nanoparticles, Figure 4c shows that the adsorption mass of the 20-nm AuNPs is greater than the 12-nm AuNPs for all salt concentrations. Importantly, for the 12-nm AuNPs, the adsorbed mass as determined by QCM approaches zero at salt concentrations near and above 15 mM,

whereas the 20-nm AuNPs exhibit "selective" adsorption at the same salt conditions. This selectivity will be demonstrated by directly imaging and counting AuNPs in the next section.

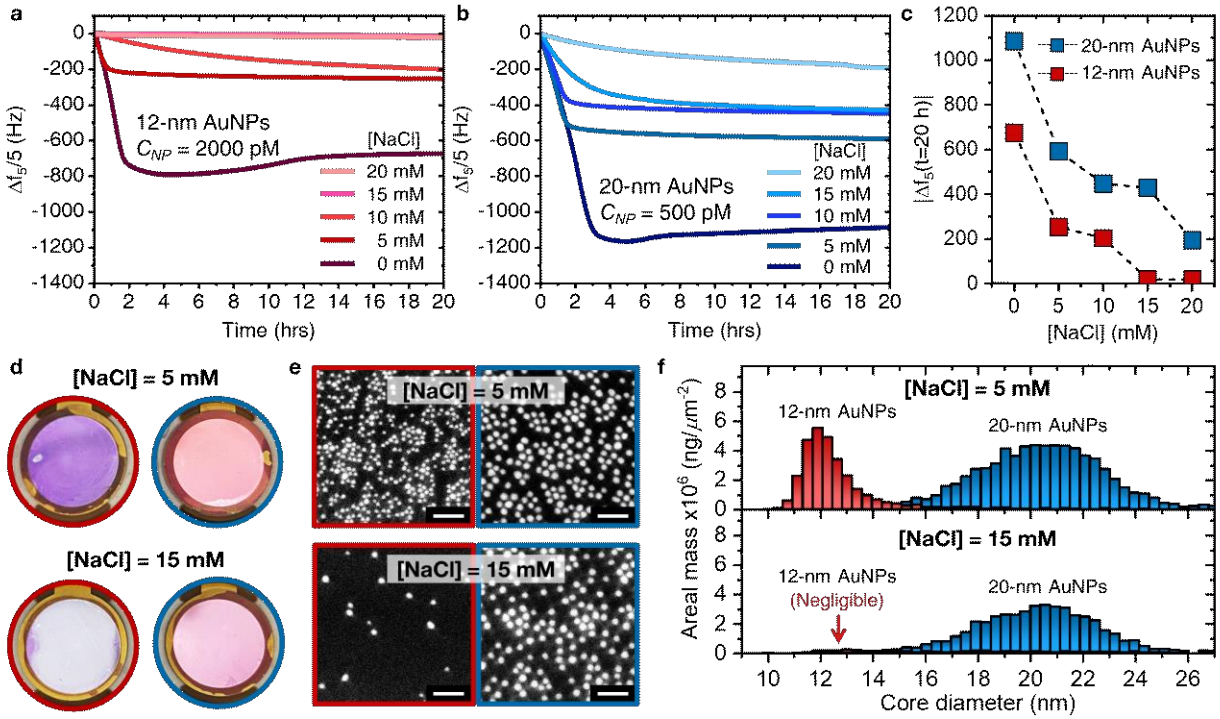

Figure 4. Salt-mediated, size-dependent adsorption of PEGylated AuNPs to PEL brush. The real-time change in the 5th overtone resonant frequency during the AuNP adsorption with **(a)** 12-nm and **(b)** 20-nm core diameter at various salt concentrations. **(c)** Absolute change in the resonant frequency of 12-nm and 20-nm AuNP adsorption at t = 20 hrs as a function of salt concentration. **(d)** Photos of QCM-D sensors and **(e)** SEM images of adsorbed AuNPs. Red (left) and blue (right) represent 12-nm and 20-nm AuNPs, respectively. The scale bars in SEM images are 100 nm. **(f)** Areal mass density distribution of adsorbed AuNPs derived from SEM images.

To quantitatively investigate the size-selective adsorption of nanoparticles on PEL brushes, post-adsorption scanning electron microscopy (SEM) analysis was conducted for the 12-nm and 20-nm AuNPs adsorbed at 5 mM and 15 mM salt concentrations after QCM-D for 20 hrs. SEM images for other salt concentrations are presented in Figure S4. As shown in Figure 4d, the extent

of nanoparticle adsorption can be qualitatively assessed by visually inspecting the color of the QCM sensor surface which is gray before nanoparticle adsorption. At 5 mM, the surface color is purple and pink for the 12-nm and 20-nm AuNPs indicating significant nanoparticles adsorbed onto the PEL brushes. The color difference reflects the difference in core diameter and areal density of AuNPs. At 15 mM, the surface with 20-nm AuNPs remains the same color (pink), whereas the surface with 12-nm AuNPs turned gray, characteristic of a PEL brush-coated QCM sensor before exposure to AuNPs. This visual observation suggests that only the larger 20-nm AuNPs were able to absorb at 15 mM. This qualitative observation is correspondingly confirmed by SEM image analysis. As shown in Figure 4e, at 5 mM, nanoparticles are densely adsorbed regardless of size. However, at 15 mM, very few of the 12-nm AuNPs are adsorbed on the PEL brush.

To quantify this observation, SEM image analysis is performed to determine the areal mass density of adsorbed nanoparticles (Figure 4f) and then compared with QCM-D results (Figure 4c). Using image analysis that measures the diameter of AuNPs, the areal mass density of PEGylated AuNPs, ρ_m, was calculated using: $\rho_m = \sum_i m_i/A = \sum_i \left(\frac{4}{3}\pi R_i^3 \rho_{Au} + \frac{4\pi R_i^2 \sigma_{PEG} M_{PEG}}{N_A}\right) / A$, where m_i is the mass of a nanoparticle, A is the area of an SEM image, R_i is the radius of a nanoparticle, ρ_{Au} is the density of gold (19.32 g/cm^3), σ_{PEG} is the grafting density of PEG chains, M_{PEG} is the molar mass of PEG chains, and N_A is the Avogadro's number. At a salt concentration of 5 mM, the areal mass density of adsorbed 20-nm AuNPs (7.0×10^{-5} ng/μm^2) was approximately 2.3 times greater than the 12-nm AuNPs (3.0×10^{-5} ng/μm^2). This result is in very good agreement with the QCM-D data, which showed a 2.3 times larger absolute change in normalized resonant frequency for the larger AuNPs. When the salt concentration is increased to 20 mM, the 12-nm AuNPs show a significant reduction in areal mass density to 0.24×10^{-5} ng/μm^2. In contrast, the 20-nm AuNPs have an areal mass density of 4.7×10^{-5} ng/μm^2, which is nearly 20 times greater than

that of the smaller nanoparticles. This improved size selectivity for the larger AuNPs is also consistent with QCM-D results, which showed a ~ 22 times greater absolute change in normalized resonant frequency for the larger AuNPs. In summary, using real-time monitoring with QCM-D and post-adsorption SEM image analysis, we demonstrate that the thermodynamics of AuNP electrostatic adsorption can be regulated by salt concentration. Also, while larger nanoparticles are preferentially adsorbed at all salt concentrations, size selectivity increases significantly at higher salt concentrations.

Interpretation of stronger adsorption by larger nanoparticles. The change in free energy of nanoparticle adsorption to a polymer brush, ΔG_{ads}, is given by $\Delta G_{ads} = \Delta H_{ads} - T\Delta S_{ads}$, where ΔH_{ads} is the change in enthalpic interactions, T is temperature, ΔS_{ads} is the change in entropy after adsorption. Based on the DLVO theory, the enthalpic interaction can be described by the electrostatic, H_{el}, and Van der Waals (VdW), H_{VdW}, attraction. When a nanoparticle is interacting with a flat surface, the free energy resulting from electrostatic and VdW attractive forces can be expressed as: $H_{NP-Poly} = H_{el} + H_{VdW} = \varepsilon\psi_{+}\psi_{-}R_{NP}exp\left(-\frac{h}{\lambda}\right) - \frac{AR_{NP}}{6h}$, where ε is the medium dielectric constant, ψ is surface charge, R_{NP} is nanoparticle radius, h is separation distance, λ is Debye length, and A is Hamaker constant. According to the above formula, the PEL brush-nanoparticle enthalpic attraction is proportional to the size of the nanoparticle. Therefore, under the same conditions, larger nanoparticles have a stronger attraction for the surface and have the potential to be selectively adsorbed. However, this description only applies to nanoparticles interacting with a flat surface. Mims *et al.* recently reported a computational study regarding nanoparticle interactions with a polymer brush under favorable interactions in a good solvent.[38] They modeled the enthalpic interactions of polymer brush monomers and a nanoparticle as: $H_{NP-Poly} \sim 2\pi r_m^2 R_{NP}$ where r_m is the monomer radius. We note that the enthalpic interaction is

also proportional to the size of the nanoparticle, which is consistent with the theoretical prediction of flat surface-nanoparticle interactions. Intuitively, the number of surface area elements of a nanoparticle that can interact with the polymer brush monomers is proportional to the size of the nanoparticle, such that larger nanoparticles exhibit greater attractive forces.

The entropy of adsorption, S_{ads}, can also be understood similarly. When nanoparticles adsorb to a PEL brush, water molecules, and counterions are released into the solution, leading to an increase in the system translational entropy that compensates for the decreases in the translational entropy of nanoparticles and conformational entropy of the PEL brush. The number of released water and counterions is proportional to the number of surface area elements that bond to the PEL brush monomers. Thus, larger nanoparticles are more advantageous for adsorption because they increase the overall system entropy through adsorption with a PEL brush. In summary, the larger the nanoparticle, the greater the enthalpic attraction and the higher the system entropy, making the adsorption of large nanoparticles more thermodynamically stable and attractive for selective adsorption from a mixture of nanoparticles.

Size-Selectivity of Larger AuNPs from a Bimodal Mixture. To demonstrate the selective adsorption capacity of a PEL brush for larger nanoparticles, we investigated the adsorption of 12-nm and 20-nm PEGylated AuNPs from a bimodal mixture for salt concentrations ranging from 0 mM to 20 mM. PEL brush surfaces were immersed in solutions containing 2000 pM and 500 pM of 12-nm and 20-nm AuNPs, respectively, for 48 h. Figure 5a shows the SEM images of adsorbed AuNPs at salt concentrations of 0 mM, 5 mM, 10 mM, 15 mM, and 20 mM. At 0 mM, the surface contains both 12-nm and 20-nm AuNPs. The number fraction of 20-nm AuNPs increases as the salt concentration increases which confirms the size-selective adsorption for larger nanoparticles in the monomodal studies shown in Figure 4. By binning AuNPs from 8

nm (red) to 28 nm (blue), Figure 5b visually shows how the number fraction of 20-nm AuNPs increases as salt concentration increases. At salt-free conditions, both larger and smaller AuNPs coexist on the surface, although a greater number of 12 nm AuNPs (red) is apparent. However, as the salt concentration increases to 20 mM, the larger AuNPs (turquoise and blue) become dominant, indicating that the PEL brush selectively adsorbs larger nanoparticles.

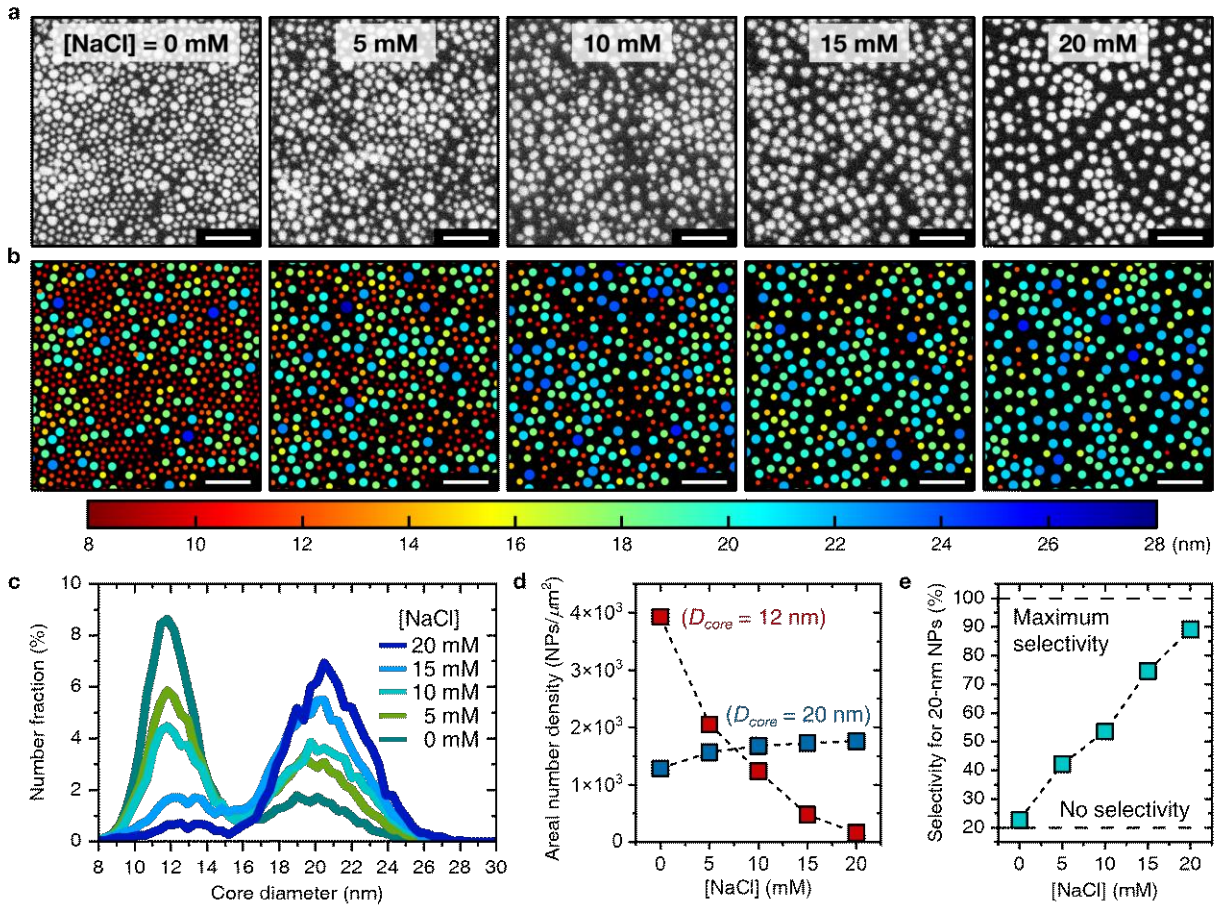

Figure 5. Salt-mediated adsorption from a bimodal mixture of PEGylated AuNPs to the PEL brush. (a) Raw SEM images and **(b)** analyzed SEM images indicate the size of the adsorbed AuNPs from a bimodal mixture (2000 pM and 500 pM of 12-nm and 20-nm AuNPs, respectively) as a function of salt concentration. The scale bars in SEM images are 100 nm. **(c)** Size distribution of adsorbed AuNPs. **(d)** The areal number density of 12-nm and 20-nm AuNPs as a function of salt concentration. **(e)** Adsorption selectivity for 20-nm AuNPs (number fraction of 20-nm AuNPs in SEM images) as a function of salt concentration.

We further investigated the size-selectivity of the PEL brush by quantifying the size distribution of AuNPs using SEM image analysis. Figure 5c shows the size distribution of adsorbed AuNPs at various salt concentrations. Under salt-free conditions, the number fraction of smaller AuNPs dominates (light purple). As salt concentration increases, the number fraction of 12-nm AuNPs decreases and that of the 20-nm AuNPs increases until there are predominately larger AuNPs on the surface at 20mM (dark purple). We further investigated the capacity of the PEL brush to capture the larger 20-nm AuNPs. The total number for both sizes was calculated by integrating each distribution (Figure S5). Figure 5d shows that the PEL brush can adsorb ~4000 12-nm AuNPs and ~1300 20-nm AuNPs per μm^2 in a salt-free solution. As expected, the number of 12-nm AuNPs (red) monotonically decreases as salt concentration increases, and at 20 mM, only ~160 AuNPs per μm^2 are adsorbed. In contrast, the number of 20-nm AuNPs increases as salt concentration increases. We attribute this behavior to the larger number of 12-nm AuNPs which adsorb before the larger 20-nm AuNPs at low concentrations when both AuNPs strongly adsorb. However, at higher salt concentrations, thermodynamic equilibrium appears to dominate as the attraction for the smaller AuNPs becomes relatively weaker. Further studies of the kinetics of adsorption are needed to further explore this observation.

Lastly, Figure 5e shows the selectivity for 20-nm AuNPs (*i.e.*, the number fraction for 20-nm) as a function of salt concentration. The selectivity for 20-nm AuNPs in a salt-free solution is ~ 20 %, reflecting the initial mixing ratio of 500 pM / 2000 pM for 20-nm to 12-nm nanoparticles. This indicates that selective adsorption is not observed at 0 mM. Significantly, the selectivity for 20-nm AuNPs increases monotonically, reaching ~ 90 % at a salt concentration of 20 mM. Despite having 4 times more small nanoparticles in the solution of AuNPs, ~ 90 % selectivity for large

nanoparticles demonstrates that size separation induced by selective adsorption by the PEL brush is highly efficient.

Narrowing the Size Distribution from an Initial AuNP Solution. After successfully isolating 20-nm AuNPs from a bimodal mixture, a more significant challenge is to demonstrate separation from a monomodal mixture prepared from a one-pot synthesis targeting 12-nm AuNPs. As shown in Figure 4f, the size distribution of 12-nm AuNPs contains a small number of nanoparticles that are much larger (*e.g.*, >15 nm) than the average size of 12 nm. Although this tail represents a small fraction of the total, this concentration of large nanoparticles can limit their use in applications that require highly uniform nanoparticle sizes to deliver precise properties. Thus, we investigated whether the nanoparticle size distribution could be narrowed by removing these larger nanoparticles using a PEL brush.

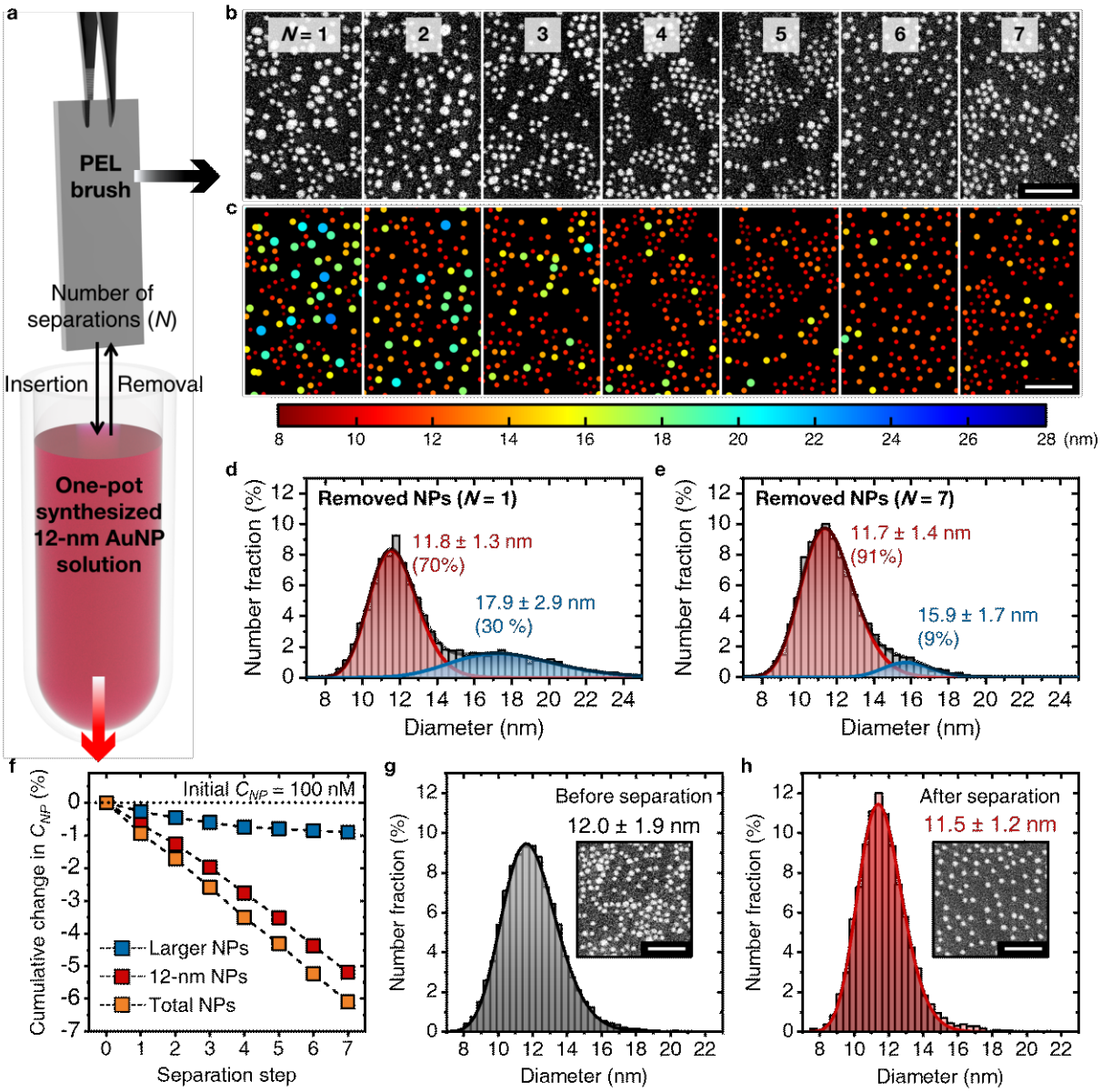

Figure 6. Removal of large nanoparticles from an initial AuNP solution. (a) Schematic of the removal strategy for initial AuNP solution using PEL brushes. **(b)** Raw SEM images and **(c)** analyzed SEM images indicate the sizes of adsorbed AuNPs as a function of iterative separation steps. Size distribution of AuNPs removed in the **(d)** 1st and **(e)** 7th separation steps. **(f)** Calculated cumulative change in the nanoparticle concentration, C_{NP}, with increasing number of separation steps. Size distribution of AuNPs **(g)** before and **(h)** after the separation with the PEL brushes. The scale bars in SEM images are 100 nm.

Larger AuNPs from a monomodal mixture were removed by sequential exposure to a PEL brush surface. As represented in Figure 6a, 5 mL of a concentrated 12-nm AuNP solution (C_{NP} = 100 nM) was adjusted to a salt concentration of 10 mM as represented by the red vial. Subsequently, four ~ 5 cm^2 wafers with PEL brush surfaces were immersed in this solution and replaced with new surfaces every 24 hours. The nanoparticles adsorbed from the solution onto the PE surfaces were imaged by SEM for the 7 separation steps, Figures 6b and 6c. Notably, in the 1st separation, a significant number of the adsorbed AuNPs are much larger than 12 nm. Moreover, the number fraction of large AuNPs monotonically decreases as the number of separation steps increases. Based on the image analysis shown in Figure 6c, the size distribution of the removed AuNPs was determined as a function of separation steps (Figures 6d and 6e). In the 1st separation step, the size distribution of the removed AuNPs exhibits two distinct distributions: 70 % of 11.8-nm (red) and 30 % of 17.9-nm AuNPs (blue). By the 7th separation, the fraction and average diameter of larger AuNPs are reduced to 9% and 15.9 nm. This observation indicates that larger nanoparticles are preferentially removed from the solution, resulting in a solution enriched in the smaller 12-nm nanoparticles.

Based on the areal number density of removed AuNPs and the area of PEL brushes used in each separation step, we calculated the change in C_{NP} on the AuNP solution as a function of separation steps, Figure 6f. The concentration of large AuNPs monotonically decreases and reaches a 1 % reduction after 7 steps. This implies that the initial AuNP solution contains ~1 % of 18 ± 3 nm AuNPs, and they are removed after 7 separation steps. We note that ~6 % of the 12-nm particles are lost through this separation process, which implies that we can obtain ~94 nM of 12-nm AuNP solution by removing ~1 nM of large AuNPs from the 100 nM initial solution. The outcome of this separation process is demonstrated by comparing the size distribution of AuNPs before and after

the 7 separation steps (Figures 6g and 6h). The presence of large AuNPs in the initial synthesis broadens the size distribution, such that the initial AuNPs have an average size of 12.0 ± 1.9 nm. After completing 7 separation steps, the average size of the AuNPs becomes smaller with a narrower size distribution, 11.5 ± 1.2 nm, consistent with the selective removal of larger nanoparticles. This study shows that PEL brushes are effective at narrowing the nanoparticle distribution from monomodal nanoparticle solution.

CONCLUSIONS

In conclusion, we demonstrated that the electrostatic adsorption of PEGylated AuNPs to oppositely charged PEL brushes is highly dependent on the nanoparticle size, and the selectivity is finely controlled by salinity. The quaternized P2VP brushes favor the adsorption of larger nanoparticles at all salt concentrations. Above a certain salt concentration, the adsorption of smaller nanoparticles is negligible, and only larger nanoparticles are adsorbed. The presence of salt changes the free energy of electrostatic adsorption, which sets the condition for size-selective adsorption of larger nanoparticles. Using a bimodal mixture of small and large nanoparticles, size selection was further demonstrated with selective adsorption of larger nanoparticles by up to 90% of the larger nanoparticles. Selective adsorption of larger nanoparticles by PEL brushes also selectively reduces the size dispersity of an as-synthesized, nearly monodisperse nanoparticle solution by preferentially removing the larger nanoparticles. In our previous study, we showed that selective adsorption of small nanoparticles is possible by controlling the pH-dependent interactions between nanoparticles and a weak PEL brush. Together with the results of this study, we demonstrate a versatile approach using polymer brushes to separate nanoparticles below and above a target size.

METHODS

Materials. A symmetric PS-*b*-P2VP block copolymer with a number-average molecular weight, M_n, of 45-*b*-49 kg/mol (PDI = 1.07), a ω-hydroxy-terminated polystyrene (PS-OH) with an M_n of 18.5 kg/mol (PDI = 1.01), and a ω-thiol-terminated poly(ethylene glycol) methyl ether (mPEG-SH) with an M_n of 2 kg/mol (PDI = 1.05) were purchased from Polymer Source. Methyl iodide (99%), sodium chloride (≥ 99%), sodium citrate tribasic dihydrate (≥ 99%), and gold(III) chloride trihydrate ($HAuCl_4 \cdot 3H_2O$, ≥ 99.9%) were purchased from Sigma-Aldrich.

Preparation of PEL brushes. The positively charged PEL brushes were synthesized by converting pyridine groups of P2VP brushes into NMP^+ followed by ion exchange from iodide to chloride. The method for the preparation of the neat P2VP brush is described in our previous paper.[41] Briefly, PS-*b*-P2VP 45-b-49 kg/mol is spin-coated onto PS-OH 18.5 kg/mol grafted Si wafers and QCM-D sensors and thermally annealed at 170 °C for 24 hrs under vacuum to create BCP bilayer lamellae. The BCP bilayer lamellae were sonicated with methanol to exfoliate the outmost layer, resulting in the creation of a 10-nm-thick P2VP brush atop a 15-nm-thick PS layer at the bottom. To synthesize the PEL brushes, the BCP samples were immersed in a methyl iodide/hexane mixture with a 1:9 volumetric mixing ratio for 24 hrs to convert the pyridine groups into NMP^+ groups. The iodide counter anions were exchanged with chloride anions by soaking the PEL brushes in a 0.1 M solution of sodium chloride for 3 hrs and followed by rinsing with deionized water for 3 hrs.

Synthesis of PEGylated AuNPs. The spherical AuNPs were synthesized using established methods.[53-55] Briefly, in a 500 mL two-neck round-bottom flask, a 300 mL aqueous 1 mM $HAuCl_4 \cdot 3H_2O$ was prepared and brought to a boil under reflux and stirring. Meanwhile, a 30 mL

aqueous solution of 38.8 mM sodium citrate was prepared and rapidly injected into the $HAuCl_4$ solution under vigorous reflux and stirring. The addition of sodium citrate solution reduced the $HAuCl_4$, resulting in nucleation and growth of AuNPs to form 12-nm spherical nanoparticles. To synthesize 20-nm AuNPs, a seeded growth of 12-nm AuNPs was performed. The 50 mL of 12-nm AuNPs solution was added to 300 mL of 2.2 mM sodium citrate solution in a 500 mL two-neck round-bottom flask. The solution temperature was set at 90°C and allowed to reach equilibrium for 1 hr under stirring. Subsequently, 2 mL of 25 mM $HAuCl_4 \cdot 3H_2O$ solution was rapidly injected stepwise 5 times at 30 min intervals for complete growth of AuNPs. To perform the PEGylation, 10 mL of 5 mM mPEG-SH solution was added to AuNP solutions and vigorously stirred overnight. The final solutions were rinsed with deionized water 5 times using a centrifuge to remove residual mPEG-SH chains and sodium citrate. After the last centrifugation, AuNPs were redispersed in 50 mL of deionized water, which produced ~0.1 wt% AuNP stock solutions.

Characterization of PEL brush Surfaces. The surface topography of PEL brushes was characterized using AFM (Dimension Icon AFM, Bruker) in tapping mode with probes (HQ: NSC15/Al BS, MikroMasch) that have a resonance frequency of 325 kHz, a force constant of 40 N/m, and a radius of 8 nm. For image scanning, the scan rate, integral gain, proportional gain, and amplitude setpoint were set to 1.00 Hz, 1.20, 6.00, and 500 mV, respectively. XPS analysis was performed using a VersaProbe 5000 instrument equipped with a monochromatic Al Kα source to investigate the charge state and ion species of PEL brush surfaces.

Characterization of Out-of-plane Brush Structure. To investigate the interior structure of the PEL brushes, XRR experiments were performed using the Dual-Source and Environmental X-ray Scattering (DEXS) facility at the University of Pennsylvania. The data were collected using a GeniX3D beam source (8 keV, Cu Ka, wavelength = 1.54 Å) and a PILATUS 1 M detector. The

sample size is 1 × 3 cm^2 and the beam size is 8 × 0.1 mm^2, and data were measured at a 363 mm sample-to-detector distance by changing the angle of incidence from 0° to 2° at 0.005° intervals for 60 s. The XRR data were analyzed utilizing the REFLEX software.[63]

Characterization of AuNPs. The AuNP diameter was determined by performing transmission small angle X-ray scattering with the DEXS facility at the University of Pennsylvania. The data were collected using the same beam source and detector as described above. AuNP solutions were placed in 1.5 mm diameter glass capillaries and measured. To obtain data over a wide q-range, data were obtained at sample-to-detector distances of 363 mm and 2520 mm and combined. The AuNP stability and concentrations were characterized with UV-vis-NIR spectroscopy (Varian Cary 5000 UV-Vis-NIR Spectrophotometer). The ζ-potential of AuNPs depending on salt concentration was obtained using a Zetasizer Nano ZS, Malvern Panalytical. The grafting density of PEG chains on the AuNP surface was quantified by thermogravimetric analysis (SDT 650, TA Instruments). The SEM images of adsorbed AuNPs on the PEL brushes were obtained using a JEOL-7500F.

Characterization of PEL brushes in Aqueous Solutions. *In situ* measurements of the brush heights as a function of salt concentration were performed using a custom-made liquid chamber mounted on an ellipsometer (J.A. Woollam Co., alpha-SE). The dehydration and ion association of PEL brushes as a function of the salt concentration was monitored using a Q-sense Analyzer at 21.0 °C. The brush preparation was performed on SiO2 (50 nm)-coated QCM-D sensors (Nanoscience Instruments, Qsensors QSX 303) for the quartz crystal microbalance with dissipation (QCM-D) experiments. The ζ-potentials of the PEL brushes were obtained using Delsa Nano C Particle Analyzer as a function of salt concentration.

***In situ* Monitoring of AuNPs Adsorption on PEL brushes.** QCM-D experiments were performed to investigate the AuNP adsorption kinetics and thermodynamics. The data were

collected using the same sensors and the instrument as described above. The flow rate and temperature of AuNP solutions were fixed at 0.2 mL/min and 21.0 °C, respectively.

ASSOCIATED CONTENTS

The Supporting Information is available free of charge

Effect of methyl iodide concentration on the BCP thin film stability; FT-IR spectra of O-H stretching vibrations; Characterization of PEGylated AuNPs using TGA and UV-vis spectra; AuNPs adsorbed to polyelectrolyte brushes on the QCM sensors; Analysis of size selectivity for 20-nm AuNP adsorption in a bimodal mixture. (PDF)

AUTHOR INFORMATION

Corresponding Authors

Karen I. Winey - Department of Chemical and Biomolecular Engineering and Department of Materials Science and Engineering, University of Pennsylvania, Philadelphia, Pennsylvania 19104, United States

Email: winey@seas.upenn.edu

Russell J. Composto - Department of Materials Science and Engineering, University of Pennsylvania, Philadelphia, Pennsylvania 19104, United States

Email: composto@seas.upenn.edu

Authors

Ye Chan Kim - Department of Materials Science and Engineering, University of Pennsylvania, Philadelphia, Pennsylvania 19104, United States

Son Hoang - Department of Materials Science and Engineering, University of Pennsylvania, Philadelphia, Pennsylvania 19104, United States

Author Contributions

K.I.W and R.J.C supervised the project. Y.C.K principally performed all experiments and data analysis. S.H assisted with the experiments. Y.C.K prepared figures and manuscript, and K.I.W and R.J.C revised the draft.

Notes

The authors declare no competing financial interests.

ACKNOWLEDGEMENTS

R.J.C., K.I.W., S.H., and Y.C.K. acknowledge funding from the National Science Foundation (NSF-CBET-2034122). The authors acknowledge the use of facilities supported by the Laboratory for Research on the Structure of Matter and the NSF through the University of Pennsylvania Materials Research Science and Engineering Center (MRSEC) DMR-2309043. The authors also gratefully acknowledge Prof. Daeyeon Lee for supporting *in situ* ellipsometry and QCM-D experiments.

REFERENCES

1. Haes, A. J.; Van Duyne, R. P., A nanoscale optical biosensor: sensitivity and selectivity of an approach based on the localized surface plasmon resonance spectroscopy of triangular silver nanoparticles. *J. Am. Chem. Soc.* **2002,** *124* (35), 10596-10604.
2. Farka, Z.; Jurik, T.; Kovar, D.; Trnkova, L.; Skládal, P., Nanoparticle-based immunochemical biosensors and assays: recent advances and challenges. *Chem. Rev.* **2017,** *117* (15), 9973-10042.
3. Loiseau, A.; Zhang, L.; Hu, D.; Salmain, M.; Mazouzi, Y.; Flack, R.; Liedberg,

B.; Boujday, S., Core–shell gold/silver nanoparticles for localized surface plasmon resonance-based naked-eye toxin biosensing. *ACS Appl. Mater. Interfaces* **2019,** *11* (50), 46462-46471.
4. Pan, J.-A.; Skripka, A.; Lee, C.; Qi, X.; Pham, A. L.; Woods, J. J.; Abergel, R. J.; Schuck, P. J.; Cohen, B. E.; Chan, E. M., Ligand-Assisted Direct Lithography of Upconverting and Avalanching Nanoparticles for Nonlinear Photonics. *J. Am. Chem. Soc.* **2024,** *146* (11), 7487-7497.
5. Liu, J.; Nero, M.; Jansson, K.; Willhammar, T.; Sipponen, M. H., Photonic crystals with rainbow colors by centrifugation-assisted assembly of colloidal lignin nanoparticles. *Nat. Commun.* **2023,** *14* (1), 3099.
6. Stratakis, E.; Kymakis, E., Nanoparticle-based plasmonic organic photovoltaic devices. *Mater. Today* **2013,** *16* (4), 133-146.
7. Voros, M.; Galli, G.; Zimanyi, G. T., Colloidal nanoparticles for intermediate band solar cells. *ACS nano* **2015,** *9* (7), 6882-6890.
8. Reineck, P.; Brick, D.; Mulvaney, P.; Bach, U., Plasmonic hot electron solar cells: the effect of nanoparticle size on quantum efficiency. *J. Phys. Chem. Lett.* **2016,** *7* (20), 4137-4141.
9. Gravelsins, S.; Park, M. J.; Niewczas, M.; Hyeong, S.-K.; Lee, S.-K.; Ahmed, A.; Dhirani, A.-A., Large emergent optoelectronic enhancement in molecularly cross-linked gold nanoparticle nanosheets. *Comm. Chem.* **2022,** *5* (1), 103.
10. Talapin, D. V.; Lee, J.-S.; Kovalenko, M. V.; Shevchenko, E. V., Prospects of colloidal nanocrystals for electronic and optoelectronic applications. *Chem. Rev.* **2010,** *110* (1), 389-458.
11. Kelly, K. L.; Coronado, E.; Zhao, L. L.; Schatz, G. C., The optical properties of metal nanoparticles: the influence of size, shape, and dielectric environment. *J. Phys. Chem. B* **2003,** *107* (3), 668-677.
12. Sweeney, S. F.; Woehrle, G. H.; Hutchison, J. E., Rapid purification and size separation of gold nanoparticles via diafiltration. *J. Am. Chem. Soc.* **2006,** *128* (10), 3190-3197.
13. Hanauer, M.; Pierrat, S.; Zins, I.; Lotz, A.; Sönnichsen, C., Separation of nanoparticles by gel electrophoresis according to size and shape. *Nano Lett.* **2007,** *7* (9), 2881-2885.
14. Akbulut, O.; Mace, C. R.; Martinez, R. V.; Kumar, A. A.; Nie, Z.; Patton, M. R.; Whitesides, G. M., Separation of nanoparticles in aqueous multiphase systems through centrifugation. *Nano Lett.* **2012,** *12* (8), 4060-4064.
15. Sharma, V.; Park, K.; Srinivasarao, M., Shape separation of gold nanorods using centrifugation. *Proc. Natl. Acad. Sci. U. S. A.* **2009,** *106* (13), 4981-4985.
16. Chen, G.; Wang, Y.; Tan, L. H.; Yang, M.; Tan, L. S.; Chen, Y.; Chen, H., High-purity separation of gold nanoparticle dimers and trimers. *J. Am. Chem. Soc.* **2009,** *131* (12), 4218-4219.
17. Bai, L.; Ma, X.; Liu, J.; Sun, X.; Zhao, D.; Evans, D. G., Rapid separation and purification of nanoparticles in organic density gradients. *J. Am. Chem. Soc.* **2010,** *132* (7), 2333-2337.
18. Bishop, L. D.; Landes, C. F., From a protein's perspective: elution at the single-molecule level. *Acc. Chem. Res.* **2018,** *51* (9), 2247-2254.
19. Niu, X.; Lin, Y.; Zhou, T.; Guan, Z.; Liu, L.; Guo, X.; Yao, Y.; Zhang, R., Nanoparticle capture by spherical polyelectrolyte brushes and its grading separation assisted by compressed CO2. *Ind. Eng. Chem. Res.* **2019,** *58* (20), 8886-8895.
20. Bhat, R. R.; Genzer, J.; Chaney, B. N.; Sugg, H. W.; Liebmann-Vinson, A., Controlling the assembly of nanoparticles using surface grafted molecular and macromolecular

gradients. *Nanotechnology* **2003,** *14* (10), 1145.
21. Ramezani Bajgiran, S.; Safi Samghabadi, F.; Li, S.; Conrad, J. C.; Marciel, A. B., Effects of the Ionizable Monomer Fraction on the Swelling Behavior of Weak Polyelectrolyte Brushes. *Macromolecules* **2023,** *56* (22), 9218-9228.
22. Kinjo, T.; Yoshida, H.; Washizu, H., Coarse-grained simulations of polyelectrolyte brushes using a hybrid model. *Colloid Polym. Sci.* **2018,** *296*, 441-449.
23. Li, Y.; Ko, Y.; Lin, Y.; Kiserow, D.; Genzer, J., Enhanced stability of surface-tethered diblock copolymer brushes with a neutral polymer block and a weak polyelectrolyte block: Effects of molecular weight and hydrophobicity of the neutral block. *Macromolecules* **2017,** *50* (21), 8580-8587.
24. Li, T.-H.; Robertson, M. L.; Conrad, J. C., Molecular weight and dispersity affect chain conformation and pH-response in weak polyelectrolyte brushes. *Polym. Chem.* **2021,** *12* (46), 6737-6744.
25. de Gennes, P., Conformations of polymers attached to an interface. *Macromolecules* **1980,** *13* (5), 1069-1075.
26. Lego, B.; Skene, W.; Giasson, S., Swelling study of responsive polyelectrolyte brushes grafted from mica substrates: effect of pH, salt, and grafting density. *Macromolecules* **2010,** *43* (9), 4384-4393.
27. Wang, C.-G.; Yong, H. W.; Goto, A., Effective synthesis of patterned polymer brushes with tailored multiple graft densities. *ACS Appl. Mater. Interfaces* **2019,** *11* (15), 14478-14484.
28. Smith, J. D.; Salas, L. A. P.; Kreft, C.; Hur, S.-M.; Gopalan, P., Chain End-Functionalized Dense Polymer Brushes from an Inimer Coating by SI-RAFT. *Langmuir* **2023,** *39* (23), 8267-8278.
29. Ehtiati, K.; Z. Moghaddam, S.; Daugaard, A. E.; Thormann, E., Crucial nonelectrostatic effects on polyelectrolyte brush behavior. *Macromolecules* **2021,** *54* (7), 3388-3394.
30. Azzaroni, O.; Brown, A. A.; Huck, W. T., Tunable wettability by clicking counterions into polyelectrolyte brushes. *Adv. Mater.* **2007,** *19* (1), 151-154.
31. Chernyy, S.; Järn, M.; Shimizu, K.; Swerin, A.; Pedersen, S. U.; Daasbjerg, K.; Makkonen, L.; Claesson, P.; Iruthayaraj, J., Superhydrophilic polyelectrolyte brush layers with imparted anti-icing properties: effect of counter ions. *ACS Appl. Mater. Interfaces* **2014,** *6* (9), 6487-6496.
32. Kou, R.; Zhang, J.; Chen, Z.; Liu, G., Counterion Specificity of Polyelectrolyte Brushes: Role of Specific Ion-Pairing Interactions. *ChemPhysChem* **2018,** *19* (11), 1404-1413.
33. Higaki, Y.; Inutsuka, Y.; Ono, H.; Yamada, N. L.; Ikemoto, Y.; Takahara, A., Counteranion-specific hydration states of cationic polyelectrolyte brushes. *Ind. Eng. Chem. Res.* **2018,** *57* (15), 5268-5275.
34. Ehtiati, K.; Moghaddam, S. Z.; Klok, H.-A.; Daugaard, A. E.; Thormann, E., Specific Counterion Effects on the Swelling Behavior of Strong Polyelectrolyte Brushes. *Macromolecules* **2022,** *55* (12), 5123-5130.
35. Roiter, Y.; Minko, I.; Nykypanchuk, D.; Tokarev, I.; Minko, S., Mechanism of nanoparticle actuation by responsive polymer brushes: from reconfigurable composite surfaces to plasmonic effects. *Nanoscale* **2012,** *4* (1), 284-292.
36. Christau, S.; Thurandt, S.; Yenice, Z.; Von Klitzing, R., Stimuli-responsive polyelectrolyte brushes as a matrix for the attachment of gold nanoparticles: The effect of brush thickness on particle distribution. *Polymers* **2014,** *6* (7), 1877-1896.

37. Christau, S.; Möller, T.; Yenice, Z.; Genzer, J.; von Klitzing, R., Brush/gold nanoparticle hybrids: effect of grafting density on the particle uptake and distribution within weak polyelectrolyte brushes. *Langmuir* **2014,** *30* (43), 13033-13041.
38. Mims, J. T.; Tsuna, L.; Spangler, E. J.; Laradji, M., Nanoparticles insertion and dimerization in polymer brushes. *J. Chem. Phys.* **2024,** *160* (8).
39. Kim, J. U.; O'Shaughnessy, B., Nanoinclusions in dry polymer brushes. *Macromolecules* **2006,** *39* (1), 413-425.
40. Kim, J. U.; O'Shaughnessy, B., Morphology selection of nanoparticle dispersions by polymer media. *Phys. Rev. Lett.* **2002,** *89* (23), 238301.
41. Kim, Y. C.; Composto, R. J.; Winey, K. I., pH-Mediated Size-Selective Adsorption of Gold Nanoparticles on Diblock Copolymer Brushes. *ACS nano* **2023,** *17* (10), 9224-9234.
42. Granqvist, C.; Buhrman, R., Ultrafine metal particles. *J. Appl. Phys.* **1976,** *47* (5), 2200-2219.
43. Menschutkin, N., Beiträge zur Kenntnis der Affinitätskoeffizienten der Alkylhaloide und der organischen Amine. *Z. Phys. Chem.* **1890,** *5* (1), 589-600.
44. Lim, H. S.; Lee, J.-H.; Walish, J. J.; Thomas, E. L., Dynamic swelling of tunable full-color block copolymer photonic gels via counterion exchange. *ACS nano* **2012,** *6* (10), 8933-8939.
45. Kang, Y.; Walish, J. J.; Gorishnyy, T.; Thomas, E. L., Broad-wavelength-range chemically tunable block-copolymer photonic gels. *Nat. Mater.* **2007,** *6* (12), 957-960.
46. Kambe, Y.; Arges, C. G.; Czaplewski, D. A.; Dolejsi, M.; Krishnan, S.; Stoykovich, M. P.; De Pablo, J. J.; Nealey, P. F., Role of defects in ion transport in block copolymer electrolytes. *Nano Lett.* **2019,** *19* (7), 4684-4691.
47. Arges, C. G.; Kambe, Y.; Suh, H. S.; Ocola, L. E.; Nealey, P. F., Perpendicularly aligned, anion conducting nanochannels in block copolymer electrolyte films. *Chem. Mater.* **2016,** *28* (5), 1377-1389.
48. Zaki, M. I.; Hasan, M. A.; Al-Sagheer, F. A.; Pasupulety, L., In situ FTIR spectra of pyridine adsorbed on SiO2–Al2O3, TiO2, ZrO2 and CeO2: general considerations for the identification of acid sites on surfaces of finely divided metal oxides. *Colloid Surf. A-Physicochem. Eng. Asp.* **2001,** *190* (3), 261-274.
49. Debye, V. P., Zur theorie der electrolyte. *Phys. Z.* **1923**, 185-206.
50. Hueckel, T.; Hocky, G. M.; Palacci, J.; Sacanna, S., Ionic solids from common colloids. *Nature* **2020,** *580* (7804), 487-490.
51. Seo, S. E.; Girard, M.; De La Cruz, M. O.; Mirkin, C. A., The importance of salt-enhanced electrostatic repulsion in colloidal crystal engineering with DNA. *ACS Cent. Sci.* **2019,** *5* (1), 186-191.
52. Borisov, O.; Zhulina, E., Effects of ionic strength and charge annealing in star-branched polyelectrolytes. *Eur. Phys. J. B* **1998,** *4*, 205-217.
53. Frens, G., Controlled nucleation for the regulation of the particle size in monodisperse gold suspensions. *Nat. Phys. Sci.* **1973,** *241* (105), 20-22.
54. Hill, H. D.; Mirkin, C. A., The bio-barcode assay for the detection of protein and nucleic acid targets using DTT-induced ligand exchange. *Nat. Protoc.* **2006,** *1* (1), 324-336.
55. Bastús, N. G.; Comenge, J.; Puntes, V., Kinetically controlled seeded growth synthesis of citrate-stabilized gold nanoparticles of up to 200 nm: size focusing versus Ostwald ripening. *Langmuir* **2011,** *27* (17), 11098-11105.
56. Wang, J.; Winans, R. E.; Anderson, S. L.; Seifert, S. n.; Lee, B.; Chupas, P. J.; Ren, Y.; Lee, S.; Liu, Y., In situ small-angle X-ray scattering from Pd nanoparticles formed by

thermal decomposition of organo-Pd catalyst precursors dissolved in hydrocarbons. *J. Phys. Chem. C* **2013,** *117* (44), 22627-22635.
57. Kwon, S. G.; Krylova, G.; Phillips, P. J.; Klie, R. F.; Chattopadhyay, S.; Shibata, T.; Bunel, E. E.; Liu, Y.; Prakapenka, V. B.; Lee, B., Heterogeneous nucleation and shape transformation of multicomponent metallic nanostructures. *Nat. Mater.* **2015,** *14* (2), 215-223.
58. Wu, B.; Wang, X.; Yang, J.; Hua, Z.; Tian, K.; Kou, R.; Zhang, J.; Ye, S.; Luo, Y.; Craig, V. S., Reorganization of hydrogen bond network makes strong polyelectrolyte brushes pH-responsive. *Sci. Adv.* **2016,** *2* (8), e1600579.
59. Kou, R.; Zhang, J.; Wang, T.; Liu, G., Interactions between polyelectrolyte brushes and Hofmeister ions: chaotropes versus kosmotropes. *Langmuir* **2015,** *31* (38), 10461-10468.
60. Wang, W.; Wei, Q.-Q.; Wang, J.; Wang, B.-C.; Zhang, S.-h.; Yuan, Z., Role of thiol-containing polyethylene glycol (thiol-PEG) in the modification process of gold nanoparticles (AuNPs): stabilizer or coagulant? *J. Colloid Interface Sci.* **2013,** *404*, 223-229.
61. Rahme, K.; Chen, L.; Hobbs, R. G.; Morris, M. A.; O'Driscoll, C.; Holmes, J. D., PEGylated gold nanoparticles: polymer quantification as a function of PEG lengths and nanoparticle dimensions. *RSC Adv.* **2013,** *3* (17), 6085-6094.
62. Wang, Y.; Quinsaat, J. E. Q.; Ono, T.; Maeki, M.; Tokeshi, M.; Isono, T.; Tajima, K.; Satoh, T.; Sato, S.-i.; Miura, Y., Enhanced dispersion stability of gold nanoparticles by the physisorption of cyclic poly (ethylene glycol). *Nat. Commun.* **2020,** *11* (1), 6089.
63. Vignaud, G.; Gibaud, A., REFLEX: a program for the analysis of specular X-ray and neutron reflectivity data. *J. Appl. Crystallogr.* **2019,** *52* (1), 201-213.

For Table of Contents Only